




## Electron-impact excitation of the $(5s^25p)^2P_{1/2} \rightarrow (5s^26s)^2S_{1/2}$ transition in indium: Theory and experiment

K. R. Hamilton , O. Zatsarinny , and K. Bartschat 

*Department of Physics and Astronomy, Drake University, Des Moines, Iowa 50311, USA*

M. S. Rabasović, D. Šević, B. P. Marinković , S. Dujko , and J. Atić

*Institute of Physics Belgrade, University of Belgrade, Pregrevica 118, 11080 Belgrade, Serbia*

D. V. Fursa  and I. Bray 

*Curtin Institute for Computation and Department of Physics and Astronomy, Perth, 6102 WA, Australia*

R. P. McEachran

*Plasma Research Laboratories, The Research School of Physics, Australian National University, Canberra, ACT 0200, Australia*

F. Blanco 

*Departamento de Estructura de la Materia, Física Térmica y Electrónica e IPARCOS, Universidad Complutense de Madrid, Avenida Complutense, E-28040 Madrid, Spain*

G. García

*Instituto de Física Fundamental, CSIC, Serrano 113-bis, E-28006 Madrid, Spain  
and Centre for Medical Radiation Physics, University of Wollongong, New South Wales 2522, Australia*

P. W. Stokes  and R. D. White 

*College of Science and Engineering, James Cook University, Townsville, Queensland 4810, Australia*

M. J. Brunger \*

*College of Science and Engineering, Flinders University, GPO Box 2100, Adelaide, SA 5001, Australia  
and Department of Actuarial Science and Applied Statistics, Faculty of Business and Information Science,  
UCSI University, Kuala Lumpur 56000, Malaysia*



(Received 17 May 2020; accepted 6 July 2020; published 3 August 2020)

We present angle-integrated and angle-differential cross sections for electron-impact excitation of the  $(5s^25p)^2P_{1/2} \rightarrow (5s^26s)^2S_{1/2}$  transition in atomic indium. Experimental data for six incident electron energies between 10 and 100 eV are compared with predictions from semirelativistic and fully relativistic  $B$ -spline  $R$ -matrix calculations, as well as a fully relativistic convergent close-coupling model. Agreement between our measured and calculated data is, with a few exceptions, found to be typically very good. Additionally, the agreement between the present theoretical predictions is generally excellent, with the remaining small deviations being associated with the slightly different, although still very accurate, descriptions of the target structure. Agreement between the present results and an earlier relativistic distorted-wave computation [T. Das, R. Srivastava, and A. D. Stauffer, *Phys. Lett. A* **375**, 568 (2011)] was, however, found to be marginal, particularly at 10 and 20 eV.

DOI: [10.1103/PhysRevA.102.022801](https://doi.org/10.1103/PhysRevA.102.022801)

### I. INTRODUCTION

The soft, gray metallic element indium ( $Z = 49$ ) belongs to the group-III elements of the Periodic Table. It is the first in a series of the  $5p$  elements in the Periodic Table (which ends with xenon), with the atoms of that series being characterized by their relatively small values of the dipole polarizability

( $\alpha \sim 65 a_0^3$  for indium) [1]. Indium (In) is currently used to make transparent electrodes in liquid-crystal displays (LCDs) [2], and its spectral lines, for both its neutral and ionized ( $\text{In}^+$ ) forms, are expected to be very important in modeling plasmas in which indium is a constituent. The latter is relevant, as indium is a possible candidate to replace mercury in low-pressure discharge lamps in lighting solutions [2,3]. Indeed, Ögün *et al.* [3] conducted some collisional-radiative modeling of an indium iodide-argon plasma to investigate that possible application. However, the excitation cross sections they

\*Corresponding author: michael.brunger@flinders.edu.au

employed in that study, from the method of Gryziński [4,5], are not expected to be accurate. Hence, one of the rationales behind the present study is to make a start to provide a set of accurate cross-section data, over a wide energy range [6], for use in gas-discharge and low-temperature plasma modeling [7].

Another important application of indium is that it is particularly suitable as a tracer for two-line atomic fluorescence (TLAF) thermometry measurements [8–10]. This method works by using two diode lasers with wavelengths of 410 and 451 nm, to excite the  $6s\ ^2S_{1/2}$  resonance state of indium atoms seeded into a flame. Owing to the typically greater oscillator strengths of atoms compared to molecules, strong fluorescence signals can be obtained at low excitation energies. A particular advantage of indium atoms is that its spin-orbit coupling in the  $5p$  ground state leads to an energy spacing that is about equal to  $kT$  in typical combustion environments (2000–4000 K) [8].

There is currently a paucity of electron-indium scattering data, both theoretical and experimental, available in the literature. From a theoretical perspective, we know of some very low-energy spin asymmetries, for elastic scattering and excitation of the metastable  $5p_{3/2}$  state, from the relativistic convergent close-coupling (RCCC) [11] and Breit-Pauli  $R$ -matrix [12] methods. Note that the current RCCC and  $B$ -spline  $R$ -matrix (BSR) and relativistic  $B$ -spline  $R$ -matrix (DBSR) calculations significantly extend those earlier investigations. An atomic optical model formulation, for elastic  $e$ -In differential cross sections (DCSs) and integral cross sections (ICSs), for electron energies between 10 and 100 eV, was reported in Rabasović *et al.* [13]. Finally, again for energies in the 10–100 eV range, a relativistic distorted-wave (RDW) computation for the  $5p \rightarrow 6s$  transition, at the DCS level, is available [14]. In terms of experimental measurements, there is a comprehensive set of elastic DCSs and ICSs in Rabasović *et al.* [13], while some preliminary  $5p \rightarrow 6s$  DCSs, at very forward-scattered electron angles, can be found in Rabasović *et al.* [15]. The present measurements significantly extend and supersede those earlier data [15].

Another rationale behind this work is to try and provide benchmark data for the  $5p \rightarrow 6s$  transition in indium, against which results from other methods might be tested. This is of timely importance, as atomic optical-potential approaches, which are computationally cheaper than the present close-coupling approaches, have been gaining in popularity (see, e.g., [16–18]) in recent years.

The structure of the remainder of this paper is as follows. In Sec. II, we provide computational details of our BSR, DBSR, and RCCC calculations. This section also includes relevant details of their target-structure computations. Thereafter, in Sec. III, a description of our experimental methodology, including the uncertainties in making our measurements, is provided. The approaches we adopted to extrapolate our DCS data to  $0^\circ$  and  $180^\circ$ , in order to generate the corresponding ICS at that energy, are also given in this section. In Sec. IV, the present theoretical and experimental DCSs and ICSs are described and discussed, and compared to the earlier RDW results [14] where appropriate. Finally, some conclusions from the present investigation are given in Sec. V.

## II. COMPUTATIONAL DETAILS

### A. BSR and DBSR models

The target-structure calculations and the scattering calculations in the present work were carried out in a similar manner to previous works. Hence, we only summarize the specific aspects for the present calculation below. A comprehensive overview of the  $B$ -spline  $R$ -matrix method was given by Zatsarinny and Bartschat [19]. Below we refer to the semirelativistic models as BSR- $N$  and to the fully relativistic models as DBSR- $N$ , where  $N$  indicates the number of states in the close-coupling expansion.

A first general version of the BSR computer code was published by Zatsarinny [20] and is constantly being updated. A stable version with many upgrades is publicly available from github [21], and substantial efforts are underway to make it generally accessible via the AMP-Gateway [22]. The DBSR calculations are based on the work described in [23], and we are currently working to make that code available as well.

As always, the first ingredient for a collision calculation is the description of the target structure. In the present case, we used the MCHF [24], GRASP2 [25], and DBSR\_HF [26] atomic structure codes to generate bound orbitals for the  $\text{In}^+$  positive ion, either just for the ground state with dominant configuration  $(5s^2)\ ^2S$  or also for the first two excited states with dominant configurations  $(5s5p)^{3,1}P^o$ , respectively. We then ran the (D)BSR code in the bound-state mode [27], which generates multiconfiguration expansions of the states for neutral In. Depending on the number of  $\text{In}^+$  states, we label these models “(d)bsr\_cc\_01” and “(d)bsr\_cc\_03,” respectively. All of the production collision calculations were carried out with the structure obtained with the (d)bsr\_cc\_03 ansatz.

While the above procedure can generate a large number of both physical and pseudostates (the individual classifications depend on whether or not the orbitals fit into the  $R$ -matrix box), an even more accurate target description can be obtained by adding a few optimized configurations as “perturbors” to the multiconfiguration expansions. Specifically, we added the  $(5s5p^2)^4P, ^2D, ^2P, ^2S$  terms in all models and, furthermore, the  $5p^3$  states in the “cc\_03” model, in order to ensure that the important  $p^2$  configuration was included properly. Although elastic scattering will be considered as part of a separate paper in the future, the latter is particularly important for that collision problem since the  $5s^25p^2$  configurations lead to negative-ion bound states for the  $^3P$  configuration, while the  $^1D$  and  $^1S$  configurations lead to resonance features at very low electron energies.

Table I lists the energy levels of the lowest 22 bound states of In, as obtained in the various (D)BSR structure models and compared with the recommended NIST levels [28]. As expected, the (d)bsr\_cc\_03 expansions provide a much better target description since they already contain the significant effect of the  $p^2$  configuration. We ultimately adjusted the diagonal elements of the Hamiltonian matrix to reproduce the experimental excitation thresholds. This is a standard procedure that is fully described in Zatsarinny [20], to whom the interested reader is referred for more details. For a comparison with the experimental data presented in this paper, this adjustment is of essentially no consequence. However, it can affect the near-threshold predictions (within fractions of an

TABLE I. Binding energies (in eV) for the In target states included in the (D)BSR close-coupling expansions. Here, “Conf.” refers to the dominant configuration.

Conf.	State	NIST [28]	bsr_cc_01	Diff.	bsr_cc_03	Diff.	dbsr_cc_01	Diff.	dbsr_cc_03	Diff.
$5s^25p$	$^2P_{1/2}^o$	-5.786	-5.187	0.599	-5.739	0.047	-4.981	0.806	-5.576	0.210
$5s^25p$	$^2P_{3/2}^o$	-5.512	-4.895	0.617	-5.437	0.075	-4.736	0.749	-5.335	0.177
$5s^26s$	$^2S_{1/2}$	-2.765	-2.546	0.219	-2.677	0.087	-2.552	0.212	-2.680	0.084
$5s^26p$	$^2P_{1/2}^o$	-1.842	-1.744	0.098	-1.820	0.022	-1.724	0.118	-1.805	0.037
$5s^26p$	$^2P_{3/2}^o$	-1.805	-1.705	0.099	-1.783	0.022	-1.692	0.112	-1.771	0.033
$5s^25d$	$^2D_{3/2}$	-1.708	-1.545	0.163	-1.701	0.007	-1.539	0.169	-1.692	0.017
$5s^25d$	$^2D_{5/2}$	-1.705	-1.544	0.162	-1.701	0.004	-1.537	0.169	-1.687	0.019
$5s5p^2$	$^4P_{5/2}$	-1.450			-1.520	-0.070			-1.607	-0.157
$5s5p^2$	$^4P_{3/2}$	-1.320			-1.409	-0.089			-1.490	-0.169
$5s^27s$	$^2S_{1/2}$	-1.286	-1.222	0.064	-1.256	0.030	-1.224	0.062	-1.259	0.026
$5s5p^2$	$^4P_{3/2}$	-1.143			-1.249	-0.106			-1.315	-0.174
$5s^27p$	$^2P_{1/2}^o$	-0.968	-0.932	0.036	-0.959	0.009	-0.925	0.043	-0.954	0.014
$5s^27p$	$^2P_{3/2}^o$	-0.954	-0.918	0.036	-0.945	0.009	-0.913	0.041	-0.942	0.013
$5s^26d$	$^2D_{3/2}$	-0.945	-0.867	0.078	-0.941	0.004	-0.863	0.081	-0.938	0.007
$5s^26d$	$^2D_{5/2}$	-0.939	-0.866	0.073	-0.939	-0.001	-0.862	0.077	-0.932	0.006
$5s^24f$	$^2F_{5/2}^o$	-0.863	-0.851	0.012	-0.863	0.001	-0.851	0.013	-0.862	0.002
$5s^24f$	$^2F_{3/2}^o$	-0.863	-0.851	0.012	-0.863	0.001	-0.851	0.013	-0.862	0.002
$5s^28s$	$^2S_{1/2}$	-0.748	-0.720	0.028	-0.734	0.014	-0.721	0.027	-0.736	0.012
$5s^28p$	$^2P_{1/2}^o$	-0.600	-0.583	0.017	-0.595	0.005	-0.580	0.021	-0.594	0.007
$5s^27d$	$^2D_{3/2}$	-0.599	-0.553	0.046	-0.596	0.004	-0.551	0.048	-0.594	0.005
$5s^27d$	$^2D_{5/2}$	-0.596	-0.553	0.044	-0.595	0.002	-0.551	0.046	-0.591	0.005
$5s^28p$	$^2P_{3/2}^o$	-0.594	-0.576	0.018	-0.589	0.005	-0.574	0.020	-0.588	0.006

eV), and hence those results need to be taken with appropriate care.

The quality of our target description can be further assessed by comparing the results for the oscillator strengths, which are very important to obtain reliable absolute values for the excitation cross sections, especially for optically allowed transitions at high incident electron energies. Table II shows the comparison of oscillator strengths between our calculated results and the recommended values from the NIST database [28].

Finally, even though this is more important for elastic scattering, we mention here that the polarizability of the ground state is obtained as  $64.5 a_0^3$ , where  $a_0 = 0.529 \times 10^{-10}$  m is the Bohr radius, provided the entire spectrum of discrete and pseudostates is accounted for. This agrees well with the experimental value of Ma *et al.* [29] within their stated uncertainty ( $56.1 \pm 18.2 a_0^3$ ) and also with the high-precision calculations of Safronova *et al.* [30]. In the (D)BSR collision models, for which we show results later, the portion of the ground-state polarizability accounted for is  $26.1 a_0^3$  (BSR-22),  $56.0 a_0^3$  (BSR-100),  $61.2 a_0^3$  (BSR-224),  $29.0 a_0^3$  (DBSR-22),  $56.0 a_0^3$  (DBSR-104), and  $61.3 a_0^3$  (DBSR-214), respectively. While missing some of the polarizability would likely be a serious defect of the models when considering elastic scattering,

experience shows that it is not so critical for the calculation of excitation processes, for which the oscillator strength of the transition is most important.

The scattering calculations were carried out with fully parallelized versions of the BSR complex [20] and the corresponding DBSR package under development. In order to check the convergence of the results with the number of states included in the close-coupling expansion, we set up several scattering models. Specifically, we show results obtained in the BSR-22, BSR-100, BSR-222, DBSR-22, DBSR-104, and DBSR-214 models. In addition to the 22 states listed in Table I, the larger models included more discrete and pseudostates to account for coupling to the discrete Rydberg spectrum as well as the ionization continuum. We chose an *R*-matrix radius of  $80 a_0$  with 152 *B*-splines of order 8 for each orbital in the BSR calculation. In DBSR, we used 186 *B*-splines of the order of 8 and 9 for the small and large components of the spinors. Splines of different orders are needed here for reasons of numerical stability [31]. Also, for our DBSR calculations, a finite nuclear size was modeled with a Fermi-type model for the nucleus. This required additional splines with a narrow distance between the knots at the very small radii. These models resulted in generalized eigenvalue problems with matrix dimensions up to 175 000.

TABLE II. Oscillator strengths for the  $(5s^25p)^2P_{1/2}^o \rightarrow (5s^26s)^2S_{1/2}$  and  $(5s^25p)^2P_{1/2}^o \rightarrow (5s^25d)^2D_{3/2}$  transitions in In obtained in the (D)BSR models. “L” and “V” indicate the results obtained with the length and velocity form of the electric dipole operator, respectively.

Lower state	Upper state	NIST [28]	bsr_cc_03 (L)	bsr_cc_03 (V)	dbsr_cc_03 (L)	dbsr_cc_03 (V)
$(5s^25p)^2P_{1/2}^o$	$(5s^26s)^2S_{1/2}$	0.14	0.120	0.118	0.135	0.129
$(5s^25p)^2P_{1/2}^o$	$(5s^25d)^2D_{3/2}$	0.36	0.320	0.326	0.349	0.341

We calculated partial waves for total electronic angular momenta up to  $J_t = 24$  numerically, and then used a top-up procedure to estimate the contribution to the transition matrix elements from even higher  $J_t$ . The calculation for the external region was performed with a parallelized version of the STGF program [32].

### B. RCCC model

The RCCC method was detailed in a number of publications [33,34] with application to  $e$ -In scattering presented in [11]. Hence, only a brief overview is presented here. The In atom is modeled as a quasi-one-electron atom with an active  $p$  electron above a frozen [Kr]4d<sup>10</sup>5s<sup>2</sup> Dirac-Fock core. The core orbitals were obtained from the GRASP package [25]. The Dirac Hamiltonian for the active electron is diagonalized in a Dirac  $L$ -spinor basis [35] to model the spectrum of the In atom. Target symmetries up to  $j^\pi = 7/2^-$  were included in the calculations. There are 26 negative-energy states (relative to the In<sup>+</sup> ionic ground state) and a large number of positive-energy states that model the coupling to the ionization channels. The total number of target states is 75, with the energy of the highest positive-energy state at about 10 eV.

We included one- and two-electron polarization potentials [36,37] to more accurately account for the effect of closed shells within the quasi-one-electron model of In, and thereby improve the accuracy of the target description and scattering calculations. The static dipole polarizability of the In<sup>+</sup> ion,  $\alpha_d = 24.01 a_0^3$ , was taken from [38]. The fall-off radius of the one-electron polarization potential was optimized for each target symmetry to obtain good agreement with NIST energies [28] for the low-lying states of In. Similar to Table I for the (D)BSR models, the lowest 22 states in the RCCC model are presented in Table III. Note that states originating from  $5s5p^2$  configurations are absent in the RCCC model. The target states up to the  $(5s^28s)^2S_{1/2}$  state are well described within the RCCC model. The number and accuracy of higher-energy bound pseudostates can be easily improved by increasing the size of the underlying  $L$ -spinor basis, but proved to be unnecessary for the present study. The major difference between the number of states in the (D)BSR and RCCC models comes from the different way the square-integrable discretization is achieved with the  $B$ -splines and  $L$ -spinors, respectively.

The two-electron polarization potential does not enter the target structure calculations for the quasi-one-electron model of In, but it enters scattering calculations and effectively leads to a modified form for the oscillator strength. The fall-off radius parameter of this potential was chosen to achieve good agreement with the NIST value [28] for the  $(5s^25p)^2P_{1/2}^o \rightarrow (5s^26s)^2S_{1/2}$  transition oscillator strength. The RCCC value is equal to 0.129, which is similar to the DBSR models (cf. Table II). For this choice of the polarization potential parameters, the oscillator strength value for the  $(5s^25p)^2P_{1/2}^o \rightarrow (5s^25d)^2D_{3/2}$  transition is 0.451, which is substantially higher than in the DBSR and NIST values. The static dipole polarizability of the In atom in the RCCC(75) model is  $40.3 a_0^3$ , which is significantly lower than the experimental value of  $68.69 a_0^3$  [29]. These are indications of the remaining imperfections of the present model. As mentioned above, however, this is

TABLE III. Binding energies (in eV) for the lowest 22 states of In included in the RCCC close-coupling expansions. Here ‘‘Conf.’’ refers to the dominant configuration.

Conf.	State	NIST [28]	RCCC	Diff.
$5s^25p$	$^2P_{1/2}^o$	-5.786	-5.782	-0.004
$5s^25p$	$^2P_{3/2}^o$	-5.512	-5.521	0.009
$5s^26s$	$^2S_{1/2}$	-2.765	-2.754	-0.011
$5s^26p$	$^2P_{1/2}^o$	-1.842	-1.808	-0.034
$5s^26p$	$^2P_{3/2}^o$	-1.805	-1.773	-0.032
$5s^25d$	$^2D_{3/2}$	-1.708	-1.706	-0.002
$5s^25d$	$^2D_{5/2}$	-1.705	-1.702	-0.003
$5s5p^2$	$^4P_{3/2}$	-1.450		
$5s5p^2$	$^4P_{1/2}$	-1.320		
$5s^27s$	$^2S_{1/2}$	-1.286	-1.280	-0.006
$5s5p^2$	$^4P_{3/2}$	-1.143		
$5s^27p$	$^2P_{1/2}^o$	-0.968	-0.952	-0.016
$5s^27p$	$^2P_{3/2}^o$	-0.954	-0.939	-0.015
$5s^26d$	$^2D_{3/2}$	-0.945	-0.926	-0.019
$5s^26d$	$^2D_{5/2}$	-0.939	-0.924	-0.015
$5s^24f$	$^2F_{5/2}^o$	-0.863	-0.864	0.001
$5s^24f$	$^2F_{3/2}^o$	-0.863	-0.864	0.001
$5s^28s$	$^2S_{1/2}$	-0.748	-0.704	-0.044
$5s^28p$	$^2P_{1/2}^o$	-0.600	-0.506	-0.094
$5s^27d$	$^2D_{3/2}$	-0.599	-0.551	-0.048
$5s^27d$	$^2D_{5/2}$	-0.596	-0.550	-0.046
$5s^28p$	$^2P_{3/2}^o$	-0.594	-0.495	-0.099

not expected to be a serious issue for the calculation of the excitation process considered here.

In the scattering calculations, the set of target states is used to expand the total wave function of the  $e$ -In collision system and formulate a set of close-coupling Lippmann-Schwinger equations for the transition matrix. These equations are solved by standard techniques that include a partial-wave expansion and a reduction to a set of linear equations. Close-coupling calculations were conducted for partial waves up to  $J_t = 20$ . Account of the larger partial waves is taken with an analytical Born subtraction technique. The solution of the Lippmann-Schwinger equations enables us to determine the collision cross sections for the transition of interest. The convergence of the calculated cross sections was established by performing a number of calculations with different sizes of the underlying  $L$ -spinor basis and the inclusion of progressively more positive-energy states in the close-coupling expansion. The present calculations have been conducted with a fully parallelized MPI-OMP version of the RCCC code.

### III. EXPERIMENTAL CONSIDERATIONS

In the current experiments, we utilized an electron-scattering apparatus that has already been described in some detail previously [39,40], so that only a brief description of its features and operational performance need be given here. It consists of an oven for the production of the indium beam, a monochromator for producing the incident electron beam and an analyzer, consisting of electrostatic optical elements and a single channeltron for electron detection, to energy analyze the scattered electrons. Note that the incident electron beam

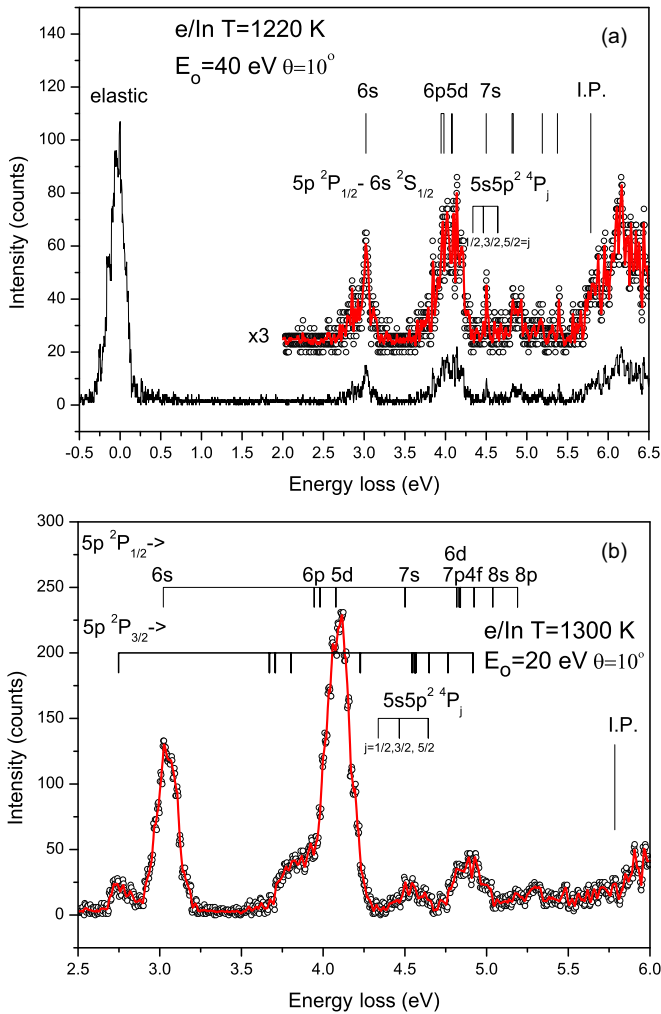


FIG. 1. Typical electron-energy-loss spectra in indium at (a)  $T = 1220$  K for  $E_0 = 40$  eV and  $\theta_e = 10^\circ$ , (b)  $T = 1300$  K for  $E_0 = 20$  eV and  $\theta_e = 10^\circ$ . Positions of the excited states are labeled according to the NIST labels of energy levels [28]. The ionization potential (I.P.) at 5.786 eV is also indicated. See text for further details.

was produced by thermionic emission from a tungsten hairpin filament, with further sets of electrostatic optical elements then collimating and transporting those electrons to the interaction region. The electron spectrometer was operated in three different modes: (i) an energy-loss mode where energy-loss spectra (see Fig. 1) were recorded for a given incident electron energy ( $E_0$ ) and scattered electron angle ( $\theta_e$ ), (ii) a mode where the energy loss was set at 0 eV (i.e., on the elastic peak) and the elastic count rate at fixed  $\theta_e$  is recorded as the incident electron energy is scanned for  $E_0 = 1.0$ – $4.4$  eV, and (iii) the energy loss is fixed at  $\sim 3.022$  eV [i.e., the excitation energy of the  $(5s^26s)^2S_{1/2}$  state of interest] and the scattered inelastic count rate is recorded as a function of  $\theta_e$  from  $2^\circ$ – $150^\circ$  at a fixed  $E_0$  (either 10, 20, 40, 60, 80, or 100 eV).

The atomic indium beam was produced by a resistively heated oven filled with 99.9% purity indium granules. Two temperatures were typically employed during the present measurements, one at approximately 1220 K and the other at about 1300 K. These operational temperatures gave metal-vapor

pressures of approximately 2.1 Pa (16 mTorr) and 8.6 Pa (65 mTorr), respectively [41]. In both cases, the effusive indium beam consists of only ground-state atoms since each temperature is well below that needed to thermally populate the first  $(5p)^2P_{3/2}$  metastable state (whose energy of 0.274 eV corresponds to a  $T \sim 3180$  K). Using the electron spectrometer in mode (i) described above, two typical energy-loss spectra at  $T = 1220$  and 1300 K are, respectively, given in Figs. 1(a) and 1(b). Note that, as we shall see in the next section, the inelastic  $6s$  differential cross sections could vary over five orders of magnitude as  $\theta_e$  changed from  $2^\circ$  to  $150^\circ$ . Therefore, the lower temperature was often utilized to make measurements of the angular distributions at the more forward-scattered electron angles, thereby avoiding saturation of the scattered electron detector (channeltron), while the higher temperature was employed at the larger scattered electron angles where the excitation cross sections were very small. There are two important points to be gleaned from Fig. 1. The first is that irrespective of the operational temperature, the  $(6s)^2S_{1/2}$  inelastic state of interest is well resolved from any of the other elastic and inelastic features. The second is that in Fig. 1(b), we can clearly also find features that originate from the excitation of the  $(5p)^2P_{3/2}$  metastable state. These latter features can only arise if the following scenario is met: an initial electron excites the  $(5p)^2P_{3/2}$  state from the ground  $(5p)^2P_{1/2}$  state, and then, before that metastable atom can decay (lifetime  $\sim 10.3$  s [42]) or leave the interaction region, a subsequent incident electron scatters from it, leading to those additional observed two-step features in Fig. 1(b).

The overall energy resolution ( $\Delta E_{\text{res}}$ ) is  $\sim 140$  meV in this work, as determined from the full width at half maximum (FWHM) of the measured  $6s$  peak in our energy-loss spectra (see Fig. 1). While allowing us to resolve the  $6s$  line from all others in the relevant spectra, it did not allow us to resolve transitions to the  $(6p)^2P_{1/2,3/2}$  states (3.945 and 3.982 eV, respectively) and to the  $(5d)^2D_{3/2,5/2}$  states (4.078 and 4.081 eV, respectively). The next weak peak in our energy-loss spectra (again, see Fig. 1) is due to the combined excitation of the  $(7s)^2S_{1/2}$  (4.501 eV) and the  $(5s5p)^2^4P_{1/2,3/2,5/2}$  states (4.337, 4.467, and 4.643 eV, respectively). The existence of other higher-lying discrete inelastic states is also visible up to the ionization potential at 5.786 eV. The incident electron-energy scale was calibrated using the spectrometer in mode (ii), and looking for a Wigner-Cusp-like feature in the elastic intensity versus energy distribution at 3.022 eV. Typically, this calibration was made at  $\theta_e = 20^\circ$ , and we believe it is accurate to about 100 meV.

The experimental procedure for the determination of our inelastic  $6s$  DCSs initially involves calibrating the angular scale for the true  $0^\circ$  scattering angle. This is achieved, for a given  $E_0$ , by setting the energy loss to 3.022 eV (i.e., for the  $6s$  peak) and then measuring the symmetry of the scattered electron intensity at small negative and positive angles about  $0^\circ$ . Once calibrated, again for a given  $E_0$  and the energy loss set at 3.022 eV, we next measured the scattered inelastic  $6s$  intensity as a function of  $\theta_e$  at fixed angles in the range  $2^\circ$ – $150^\circ$  (see Table IV). Background-intensity measurements were made at each  $\theta_e$  by moving the energy loss off 3.022 eV and to a value where no peak is observed, and measuring the signal there. This background intensity is then subtracted from

TABLE IV. Differential cross sections for the excitation of the  $6s^2S_{1/2}$  state of indium. The last row contains the angle-integrated cross sections in units of  $10^{-20}$  m<sup>2</sup>. The absolute uncertainties are indicated in parentheses.

Scattering angle (degrees)	DCS ( $\times 10^{-16}$ cm <sup>2</sup> sr <sup>-1</sup> )					
	10 eV	20 eV	40 eV	60 eV	80 eV	100 eV
2	12.5(1.6)	30.1(3.9)	45.0(6.2)	45.2(7.3)	49.9(10.6)	50.1(10.9)
4	9.2(1.2)	21.1(2.8)	24.3(3.6)	19.9(3.4)	18.3(3.4)	14.3(2.8)
6	6.10(0.83)	13.2(1.8)	11.1(1.7)	7.72(1.36)	5.17(1.01)	3.13(0.65)
8	3.73(0.52)	7.54(1.13)	4.67(0.80)	3.07(0.55)	1.44(0.28)	0.839(0.148)
10	2.32(0.35)	4.32(0.64)	2.18(0.34)	1.27(0.24)	0.555(0.099)	0.316(0.048)
20	0.266(0.041)	0.138(0.021)	0.0595(0.0103)	0.0468(0.0105)	0.0269(0.0065)	0.0090(0.0021)
30	0.0556(0.0095)	0.0527(0.0084)	0.0145(0.0035)	0.0084(0.0019)	0.0063(0.0024)	0.0040(0.0014)
40	0.0237(0.0048)	0.0173(0.0033)	0.0017(0.0009)	0.0035(0.0010)	0.0044(0.0021)	0.0026(0.0008)
50	0.0128(0.0026)	0.0026(0.0009)	0.0013(0.0008)	0.0027(0.0009)	0.0028(0.0019)	0.0022(0.0015)
60	0.0071(0.0017)	0.0024(0.0010)	0.0020(0.0009)	0.0011(0.0008)	0.0031(0.0022)	0.0025(0.0016)
70	0.0028(0.0011)	0.0012(0.0009)	0.0017(0.0009)	0.0011(0.0008)	0.0013(0.0009)	0.0025(0.0017)
80	0.0022(0.0010)	0.0032(0.0011)	0.0012(0.0008)	0.0012(0.0008)	0.0022(0.0015)	0.0019(0.0014)
90	0.0014(0.0008)	0.0015(0.0009)	0.0013(0.0009)	0.0014(0.0009)	0.0021(0.0015)	0.0040(0.0026)
100	0.00083(0.00070)	0.00072(0.00029)	0.0022(0.0010)	0.0021(0.0009)	0.00093(0.00074)	0.0041(0.0027)
110	0.0015(0.0005)	0.00043(0.00015)	0.0043(0.0012)	0.0038(0.0011)	0.0018(0.0013)	0.0043(0.0027)
120	0.0021(0.0010)	0.00107(0.00034)	0.0066(0.0017)	0.0036(0.0010)	0.0034(0.0022)	0.0045(0.0028)
130	0.0036(0.0014)	0.0039(0.0037)	0.0043(0.0014)	0.0024(0.0009)	0.00095(0.00076)	0.0046(0.0032)
140	0.0038(0.0012)	0.0023(0.0005)	0.0031(0.0011)	0.00082(0.00061)	0.0036(0.0022)	0.0041(0.0027)
150	0.0037(0.0015)	0.0054(0.0010)	0.0100(0.0022)	0.0018(0.0008)	0.0011(0.0008)	0.0054(0.0031)
ICS	0.941(0.423)	1.60(0.56)	1.53(0.54)	1.10(0.38)	0.998(0.349)	0.819(0.287)

that obtained for the  $6s$  peak in order to obtain the true  $6s$  signal.

This entire procedure is, at the required  $E_0$ , repeated three to five times and on different days, with the weighted mean of the relative DCSs of those measurements subsequently being determined. The resulting angular distribution is then multiplied by the effective path-length (or volume) correction factor [43,44], as previously determined, at the same  $E_0$ , by Rabasović *et al.* [45]. The absolute scale of that angular distribution is then determined, at 20, 40, 60, 80, and 100 eV, respectively, by measurement of the  $6s$  inelastic to elastic intensity ratios at  $10^\circ$  (for each  $E_0$ ) and then using the absolute values of the elastic DCS from Rabasović *et al.* [13]. We note that this method could not be employed at 10 eV, as no 10 eV and  $10^\circ$  elastic DCS is available in the work of Rabasović *et al.* [13]. As a consequence, the absolute scale at 10 eV is set by a generalized oscillator strength analysis [6] of its  $6s$  angular distribution in a method very similar to that of the preliminary study from Rabasović *et al.* [15]. The overall uncertainty on our DCSs is determined as the square root of the sum of the squared individual error contributions: (i) statistical uncertainties determined for each  $E_0$  and every  $\theta_e$  from the weighted mean of the relative true signal intensities; (ii) estimated uncertainty contributions due to errors in the energy-scale calibration, the effective path-length correction factor, and the calibration of the true  $0^\circ$  scattering angle; (iii) the uncertainty in the  $6s$  to elastic intensity ratios in the normalization process; and (iv) the inherited errors on the elastic DCSs from Rabasović *et al.* [13]. Values of the absolute errors in our  $6s$  DCSs, at each  $E_0$  and  $\theta_e$ , can be found in Table IV. Note that in some cases (e.g., at 20 eV and  $\theta_e = 130^\circ$ ), relatively large and somewhat anomalous errors are

found. This is due to working in regimes where the scattered intensity is weak, and the signal-to-noise characteristics are quite marginal.

Having determined our measured inelastic  $6s$  DCSs, we now need to extrapolate them to  $\theta = 0^\circ$  and  $180^\circ$ , perform an interpolation, and then undertake the appropriate integration in order to derive the  $6s$  ICSs at each energy. Two approaches were utilized to achieve that aim. In the first, we used the angular dependence predicted by our DBSR-214 theory in order to make the extrapolation, while in the second, the fitting analysis of Allen and co-workers [46,47] provided an independent self-consistency check. In all cases, the  $6s$  ICSs we obtained, from each of the aforementioned approaches, were found to be consistent with one another to within our uncertainty estimates on the ICSs. A summary of our measured ICSs and their associated errors can be found at the foot of Table IV. Note that our uncertainty estimates on the ICSs incorporate all the uncertainties on the DCS, but weighted for the  $\sin\theta$  term in the integrand when calculating those ICSs, and an additional uncertainty due to the extrapolation of our DCS to  $0^\circ$  and  $180^\circ$  in order to perform the integration at each  $E_0$ .

#### IV. RESULTS AND DISCUSSION

In Table IV and Figs. 2(a)–2(f), we present our measured  $6s$  excitation DCS for the incident electron energies (a) 10, (b) 20, (c) 40, (d) 60, (e) 80, and (f) 100 eV. Also shown in Fig. 2 are the corresponding results from our BSR-222, DBSR-22, DBSR-214, and RCCC-75 computations, as well as the results from an earlier RDW calculation [14].

There are several general observations we can make with regard to Fig. 2. First, we highlight the excellent agreement

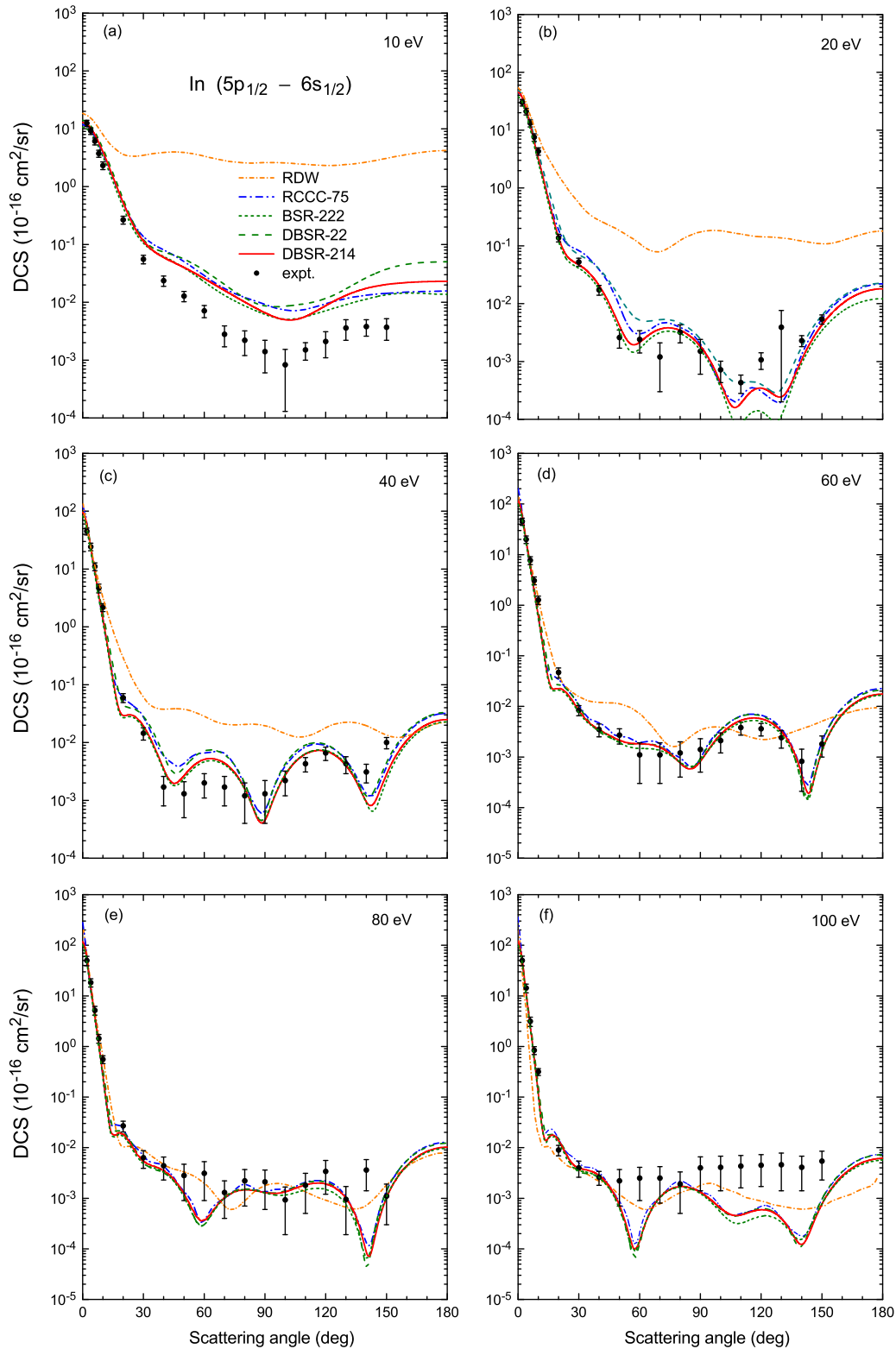


FIG. 2. Angle-differential cross section for electron-impact excitation of the  $(5s^25p)^2P_{1/2}^o \rightarrow (5s^26s)^2S_{1/2}$  transition in neutral In at incident projectile energies of (a) 10, (b) 20, (c) 40, (d) 60, (e) 80, and (f) 100 eV. Predictions from the DBSR-22, BSR-222, DBSR-214, and RCCC-75 models are compared with the present experimental data. See, also, the legend in the figure.

between our DBSR-214 and RCCC-75 theories and the present experimental data, at the more forward-scattered electron angles ( $\theta \leq 10^\circ$ ) and for all the incident electron energies in the 10–100 eV range that we studied. This is no moot point;

it is precisely these very forward angles  $\theta$  which make the major contribution to the integrand in calculating the ICS at each  $E_0$ . Thus, on the basis of this very good accord between measurement and calculation at those more forward-scattered

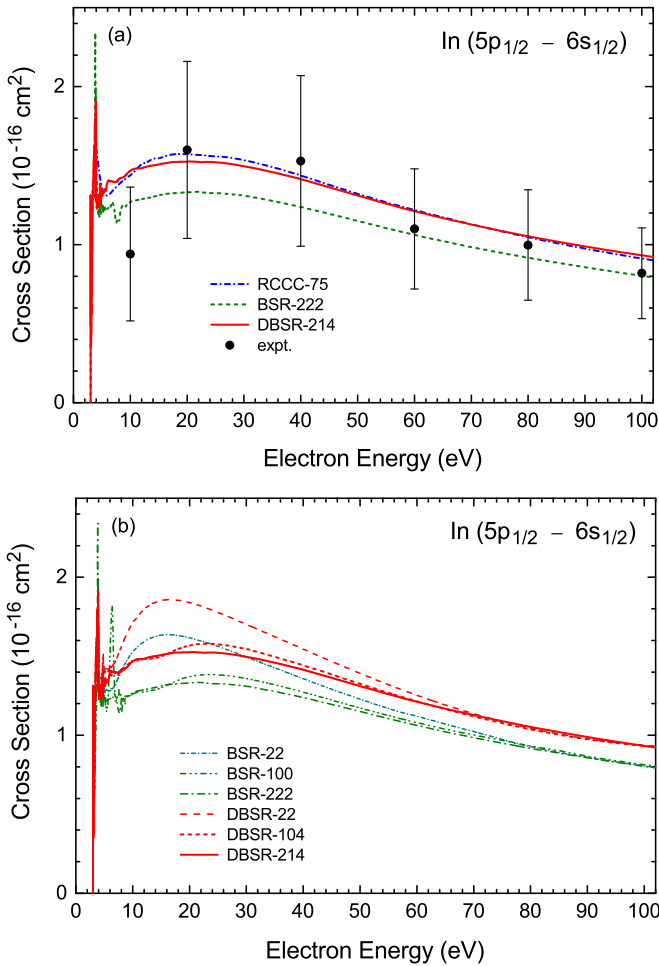


FIG. 3. Angle-integrated cross section for electron-impact excitation of the  $(5s^2 5p)^2 P_{1/2}^o \rightarrow (5s^2 6s)^2 S_{1/2}$  transition in neutral In. We show predictions from the (b) BSR-22, BSR-100, BSR-222, DBSR-22, DBSR-104, and DBSR-214 models, as well as the (a) RCCC-75 model and a comparison with the current experimental data.

electron angles, we can also safely anticipate a good level of agreement between them at the integral cross-section level of comparison (see later and Fig. 3).

Second, we highlight the very good level of accord in Fig. 2 between our RCCC-75 and DBSR-214 calculations across all  $\theta$  and at each  $E_0$  studied. This is no moot point either, as, in attempting to construct a recommended data set for this excitation process, it is vital to have two high-level calculations in such good agreement with one another. We note that where differences in our RCCC-75 and DBSR-214 computations are observed, we believe that they are attributable to the subtle differences in the target-structure descriptions in both models.

The third general observation we make relates to the RDW results. At 10 and 20 eV, they overestimate the magnitude of the present measured and calculated DCS across the entire scattered electron angular range. This is not a new observation; the limitations of the (R)DW approach to calculating inelastic DCS at lower energies are well known. By 40 eV, however, the RDW is at least correctly predicting the magnitude and angular dependence [see Fig. 2(c)] of the very

forward-angle DCS, although it continues to overestimate the magnitude of the cross section at intermediate scattered electron energies. This forward-angle behavior of the RDW persists at 60, 80, and 100 eV, so that estimates of the RDW ICS at those energies might be expected to be physical. Furthermore, it is clear from Fig. 2 that as the energy of the incident electron increases, the RDW results become in better accord with the present measured and calculated cross sections.

The final general point that we highlight is the excellent quantitative agreement between our DBSR-214 and RCCC-75 results and the present measurements for 20, 40, 60, and 80 eV impact energies and across all the scattered electron angles (see Fig. 2). In addition, we believe that at 100 eV, the level of accord is semiquantitative in nature, with the comparison we observe in Fig. 2(f) probably highlighting just how difficult it is (experimentally) in measuring very small cross-section values at middle and backward angles.

Only at 10 eV and for  $\theta > 10^\circ$  [see Fig. 2(a)] do we find a serious discrepancy in the magnitude of the DCSs between our calculations and measurement, although the shape accord between theory and experiment remains qualitatively very good. One possible experimental explanation for this discrepancy is if, despite our best efforts, our effective path-length correction factor [45] for 10 eV was a little inaccurate. From the theoretical side, the fact that the diverse calculations are in such agreement indicates that convergence with increasing number of states in the close-coupling expansion has been reached to sufficient accuracy. However, given the smallness of the cross sections, the observed discrepancy could be due to some minor systematic inaccuracy in the calculations. Nevertheless, for practical purposes, the agreement at the forward-scattering angles is such that the integrated cross section obtained from experiment and theory would be in excellent agreement.

One of the key features from the present study is the strong oscillatory nature of the angular distributions in Fig. 2. Indeed, this behavior appears to be ubiquitous in electron-metal vapor scattering, for both the elastic and discrete inelastic channels, with a few examples supporting that assertion being bismuth [40], zinc [39], sodium [48], and magnesium [49]. The oscillatory nature of any differential cross section arises from the interference, both constructive and destructive, between the various partial waves that describe the collisional behavior. In the present case of inelastic scattering, where the orbital angular momentum of the projectile necessarily has to change from the initial state to the final state in order to conserve the parity as well as the coupled electronic angular momentum ( $J$ ) of the combined target + projectile collision system, the details depend in a complex way on the interference between  $T$ -matrix elements that need to be combined with spherical harmonics in order to generate the scattering amplitudes [50] and, subsequently, the angle-differential cross section [51]. It is, therefore, generally not possible to predict either the number or the positions of the minima (maxima) in the DCS. Even though in some special circumstances and models a resemblance to elastic scattering may appear in inelastic collisions [52], and the DCS generally exhibits less structure in the angular dependence with decreasing projectile energy, drawing truly quantitative conclusions is not possible.



At the foot of Table IV and in Fig. 3(a), we present our derived  $6s$  experimental excitation ICSs. Also shown in Fig. 3(a) are the results from our BSR-222, DBSR-214, and RCCC-75 computations. Our best calculations, the RCCC-75 and DBSR-214, agree extremely well with each other and, to within the uncertainties on the experimental ICSs, they also agree very well with the measured data. Our nonrelativistic BSR-222 computation also agrees with the experimental results to within the uncertainties on those measurements, with the observed differences between it and the DBSR-214 calculation being due to the different structure model used in each case. As noted in Sec. II, both the (D)BSR and RCCC calculations appear to be well converged with the number of states included in the close-coupling expansion. Indeed, if we were to take an average of the RCCC-75 and DBSR-214 ICSs, and then calculate the standard deviation of that average from the individual computations, a discrepancy of typically less than 10% is found. We therefore ascribe the uncertainty on our RCCC-75 and DBSR-214 results to be a conservative  $\pm 10\%$ . Furthermore, that average theoretical ICS remains in very good accord, as expected, with the measured ICSs and so represents an excellent candidate for being a recommended  $6s$  integral cross section for electron-indium scattering.

In Fig. 3(b), we explicitly demonstrate the convergence properties of our BSR and DBSR calculations. This is one of the procedures recommended in [53]. As we can see from this figure, away from the near-threshold energy region, the  $6s$  ICS does not change significantly in going from our BSR-100 to BSR-222 calculations and, similarly, it does not change significantly in going from our DBSR-104 to DBSR-214 computations. These observations give us confidence in the convergence of our BSR-222 and DBSR-214 ICSs. In the near-threshold region, both our BSR and DBSR results, and our RCCC results, show peaklike structures in the ICS, which are mainly due to Feshbach resonances, and some more smoother structures, reminiscent of Wigner cusps, that are related to the opening of higher-lying channels as the incident electron energy is increased. The near-threshold structure seen in the (D)BSR calculation is very complex. To resolve the details and to check the stability with regard to even minor changes in the models, a very narrow energy grid would have to be used, followed by a thorough analysis of the partial-wave contributions and fitting of the  $T$ -matrix elements to multichannel resonance theory [54]. This is far beyond the scope of the present paper, where our main aim is to lay the groundwork for a set of recommended cross sections that can be used to produce reliable rate coefficients for modeling. For that purpose, the fine details of the resonance structure over a small energy range are irrelevant. Nonetheless, it does remain an interesting project for the future.

## V. CONCLUSIONS

We have reported on experimental and theoretical results for electron-impact excitation of the  $(5s^25p)^2P_{1/2}^o \rightarrow (5s^26s)^2S_{1/2}$  transition in neutral indium, and in doing so we have significantly extended the available cross-section database for this scattering system. Strong interference effects, both constructive and destructive, in the partial waves describing this inelastic scattering process were clearly observed in our measured and calculated angular distributions, as was their energy dependence. Generally excellent agreement was found between our highest-level RCCC-75 and DBSR-214 calculations, at both the DCS and ICS levels of comparison; and with the main exception of 10 eV and for scattered electron angles  $> 10^\circ$ , there was also very good accord found between those calculations and our measured data. Given this high level of accord between our experimental and theoretical results, we believe a recommended  $6s$  data set could be formed by taking an average, at any energy, between our RCCC-75 and DBSR-214 calculations with the uncertainty on that average result being about  $\pm 10\%$ .

Structures, near threshold, in the  $6s$  integral cross section were also found. These originate from either Feshbach resonances or are associated with the opening of higher-lying discrete excited electronic states (possibly Wigner cusps) as the incident electron energy is increased. However, more detailed calculations, beyond the scope of this study, are required before any attempt to classify them might be made. We note, additionally, that negative-ion resonance features in indium were also briefly mentioned in the review of Buckman and Clark [55].

## ACKNOWLEDGMENTS

The work of K.R.H., O.Z., and K.B. was supported by the U.S. National Science Foundation under Grants No. OAC-1834740 and No. PHY-1803844, and by the XSEDE supercomputer allocation Grant No. PHY-090031. The (D)BSR calculations were carried out on Stampede2 at the Texas Advanced Computing Center. The work of D.V.F. and I.B. was supported by the Australian Research Council and resources provided by the Pawsey Supercomputing Centre with funding from the Australian Government and the Government of Western Australia. F.B. and G.G. acknowledge partial financial support from the Spanish Ministry MICIU (Project No. PID2019-104727RB-C21) and CSIC (Project No. LINKA20085). This work was also financially supported, in part, by the Australian Research Council (Project No. DP180101655), the Ministry of Education, Science and Technological Development of the Republic of Serbia, and the Institute of Physics (Belgrade). We thank Dr. L. Campbell for his help with some aspects of this paper.

- [1] P. Schwerdtfeger and J. Nagle, *Mol. Phys.* **117**, 1200 (2019).
- [2] M. S. Rabasović, B. P. Marinković, and D. Šević, *Opt. Quantum Electron.* **50**, 236 (2018).
- [3] C. M. Ögün, W. Truong, C. Kaiser, R. Kling, and W. Heering, *J. Phys. D* **47**, 285202 (2014).

- [4] M. Gryziński, *Phys. Rev.* **138**, A336 (1965).
- [5] M. Gryziński, *Phys. Rev.* **138**, A322 (1965).
- [6] H. Tanaka, M. J. Brunger, L. Campbell, H. Kato, M. Hoshino, and A. R. P. Rau, *Rev. Mod. Phys.* **88**, 025004 (2016).
- [7] M. J. Brunger, *Int. Rev. Phys. Chem.* **36**, 333 (2017).

- [8] J. Hult, I. S. Burns, and C. F. Kaminski, *Proc. Combust. Inst.* **30**, 1535 (2005).
- [9] Q. N. Chan, P. R. Medwell, P. A. M. Kalt, Z. T. Alwahabi, B. B. Dally, and G. J. Nathan, *Appl. Opt.* **49**, 1257 (2010).
- [10] R. S. M. Chrystile, I. S. Burns, J. Hult, and C. F. Kaminski, *Opt. Lett.* **34**, 2492 (2009).
- [11] C. J. Bostock, D. V. Fursa, and I. Bray, *J. Phys. B* **45**, 181001 (2012).
- [12] K. Bartschat, *J. Phys. B* **25**, L307 (1992).
- [13] M. S. Rabasović, V. I. Kelemen, S. D. Tošić, D. Šević, M. M. Dovahnych, V. Pejčev, D. M. Filipović, E. Y. Remeta, and B. P. Marinković, *Phys. Rev. A* **77**, 062713 (2008).
- [14] T. Das, R. Srivastava, and A. D. Stauffer, *Phys. Lett. A* **375**, 568 (2011).
- [15] M. S. Rabasović, S. D. Tošić, D. Šević, V. Pejčev, D. M. Filipović, and B. P. Marinković, *Nucl. Instrum. Methods B* **267**, 279 (2009).
- [16] R. P. McEachran, F. Blanco, G. García, and M. J. Brunger, *J. Phys. Chem. Ref. Data* **47**, 033103 (2018).
- [17] R. P. McEachran, F. Blanco, G. García, P. W. Stokes, R. D. White, and M. J. Brunger, *J. Phys. Chem. Ref. Data* **47**, 043104 (2018).
- [18] R. P. McEachran, B. P. Marinković, G. García, R. D. White, P. W. Stokes, D. B. Jones, and M. J. Brunger, *J. Phys. Chem. Ref. Data* **49**, 013102 (2020).
- [19] O. Zatsarinny and K. Bartschat, *J. Phys. B: At. Mol. Opt. Phys.* **46**, 112001 (2013).
- [20] O. Zatsarinny, *Comput. Phys. Commun.* **174**, 273 (2006).
- [21] B-spline atomic r-matrix codes, <https://github.com/zatsaroi/BSR3>.
- [22] Gateway for atomic and molecular physics, <https://ampgateway.org>.
- [23] O. Zatsarinny and K. Bartschat, *Phys. Rev. A* **77**, 062701 (2008).
- [24] C. Froese-Fischer, G. Tachiev, G. Gaigalas, and M. R. Godefroid, *Comput. Phys. Commun.* **176**, 559 (2007).
- [25] P. Jönsson, X. He, C. F. Fischer, and I. P. Grant, *Comput. Phys. Commun.* **177**, 597 (2007).
- [26] O. Zatsarinny and C. F. Fischer, *Comput. Phys. Commun.* **202**, 287 (2016).
- [27] O. Zatsarinny and C. F. Fischer, *Comput. Phys. Commun.* **180**, 2041 (2009).
- [28] A. Kramida, Yu. Ralchenko, J. Reader, and NIST ASD Team, NIST Atomic Spectra Database (ver. 5.7.1), <http://physics.nist.gov/asd> (National Institute of Standards and Technology, Gaithersburg, MD, 2020).
- [29] L. Ma, J. Indergaard, B. Zhang, I. Larkin, R. Moro, and W. A. de Heer, *Phys. Rev. A* **91**, 010501(R) (2015).
- [30] M. S. Safronova, U. I. Safronova, and S. G. Porsev, *Phys. Rev. A* **87**, 032513 (2013).
- [31] C. F. Fischer and O. Zatsarinny, *Comput. Phys. Commun.* **180**, 879 (2009).
- [32] N. R. Badnell, <http://amdpp.phyd.strath.ac.uk/rmatrix>.
- [33] D. V. Fursa and I. Bray, *Phys. Rev. Lett.* **100**, 113201 (2008).
- [34] C. J. Bostock, *J. Phys. B: At. Mol. Opt. Phys.* **44**, 083001 (2011).
- [35] I. P. Grant and H. M. Quiney, *Phys. Rev. A* **62**, 022508 (2000).
- [36] D. V. Fursa and I. Bray, *J. Phys. B: At. Mol. Opt. Phys.* **30**, 5895 (1997).
- [37] D. V. Fursa, I. Bray, and G. Lister, *J. Phys. B: At. Mol. Opt. Phys.* **36**, 4255 (2003).
- [38] M. S. Safronova, M. G. Kozlov, and C. W. Clark, *Phys. Rev. Lett.* **107**, 143006 (2011).
- [39] B. P. Marinković, R. Panajotović, D. Šević, R. P. McEachran, G. García, F. Blanco, and M. J. Brunger, *Phys. Rev. A* **99**, 062702 (2019).
- [40] B. Predojević, D. Šević, B. P. Marinković, R. P. McEachran, F. Blanco, G. García, and M. J. Brunger, *Phys. Rev. A* **101**, 032704 (2020).
- [41] C. B. Alcock, V. P. Itkin, and M. Y. Horrigan, *Canad. Met. Quart.* **23**, 309 (1984).
- [42] B. K. Sahoo and B. P. Das, *Phys. Rev. A* **84**, 012501 (2011).
- [43] R. T. Brinkman and S. Trajmar, *J. Phys. E* **14**, 245 (1981).
- [44] M. J. Brunger and S. J. Buckman, *Phys. Rep.* **357**, 215 (2002).
- [45] M. S. Rabasović, S. D. Tošić, V. Pejčev, D. Šević, D. M. Filipović, and B. P. Marinković, *Facta Univ., Ser. Phys. Chem. Technol.* **6**, 119 (2008).
- [46] L. J. Allen, M. J. Brunger, I. E. McCarthy, and P. J. O. Teubner, *J. Phys. B* **20**, 4861 (1987).
- [47] M. J. Brunger, S. J. Buckman, L. J. Allen, I. E. McCarthy, and K. Ratnavelu, *J. Phys. B* **25**, 1823 (1992).
- [48] P. J. O. Teubner, J. L. Riley, M. J. Brunger, and S. J. Buckman, *J. Phys. B* **19**, 3313 (1986).
- [49] M. J. Brunger, J. L. Riley, R. E. Scholten, and P. J. O. Teubner, *J. Phys. B* **21**, 1639 (1988).
- [50] K. Bartschat and N. S. Scott, *Comput. Phys. Commun.* **30**, 369 (1983).
- [51] K. Bartschat, *Comput. Phys. Commun.* **30**, 383 (1983).
- [52] K. Bartschat and K. Blum, *J. Phys. B* **15**, 2747 (1982).
- [53] H. Chung, B. Braams, K. Bartschat, A. Csaszar, G. Drake, T. Kirchner, V. Kokoouline, and J. Tennyson, *J. Phys. D* **49**, 363002 (2016).
- [54] K. Bartschat and P. G. Burke, *Comput. Phys. Commun.* **41**, 75 (1986).
- [55] S. J. Buckman and C. W. Clark, *Rev. Mod. Phys.* **66**, 539 (1994).